GSA DATA REPOSITORY 2010012

Ancient equatorial thermokarst lakes in Ares Vallis as evidence for transient warm conditions on Mars

Nick Warner[1], Sanjeev Gupta[1], Jung-Rack Kim[2], Shih-Yuan Lin[2] and Jan-Peter Muller[2]

[1]Dept. Earth Science & Engineering, Imperial College London, South Kensington Campus, London, SW7 2AZ, [2]Mullard Space Science Laboratory, Department of Space and Climate Physics, University College London, Holmbury St Mary, Surrey, RH5 6NT

1. CTX Digital Terrain Model construction methods

2. Assessment of DTM height accuracy

3. Crater Count Methods

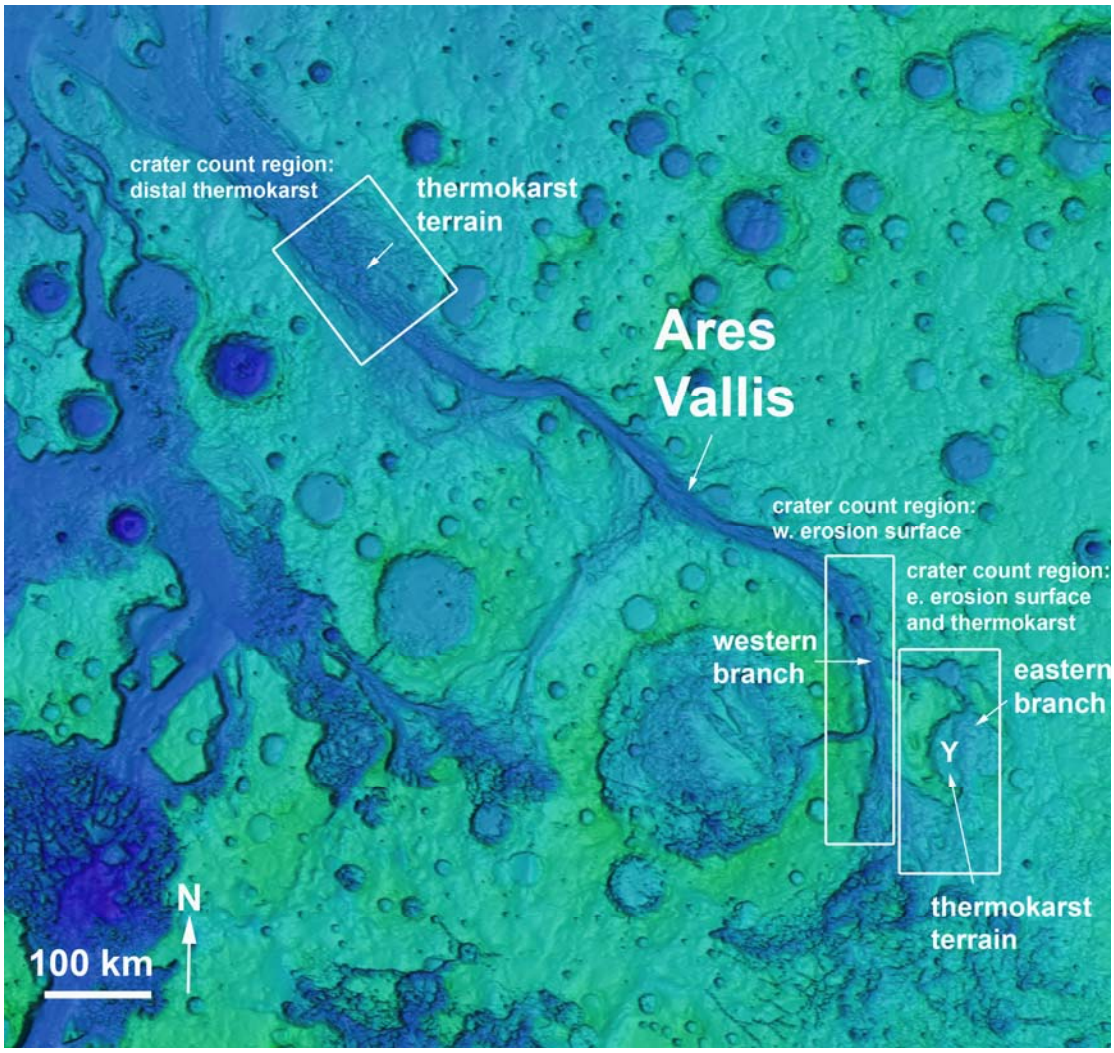

Figure DR1. MOLA topography map of Ares Vallis illustrating the location of the thermokarst terrains and flood erosion surfaces. Area of crater count study is outlined.

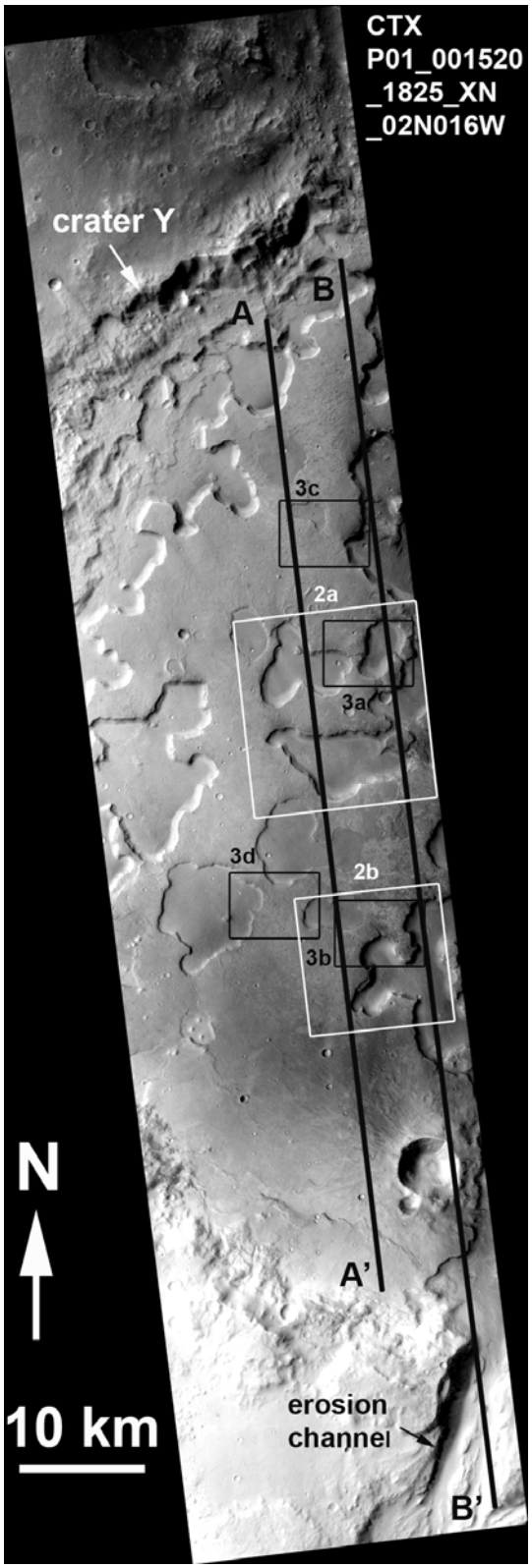
CTX
P01_001520
_1825_XN
_02N016W
crater Y
A
B
3c
2a
3a
3d
2b
3b
N
A'
10 km
erosion
channel
B'
Figure DR2a

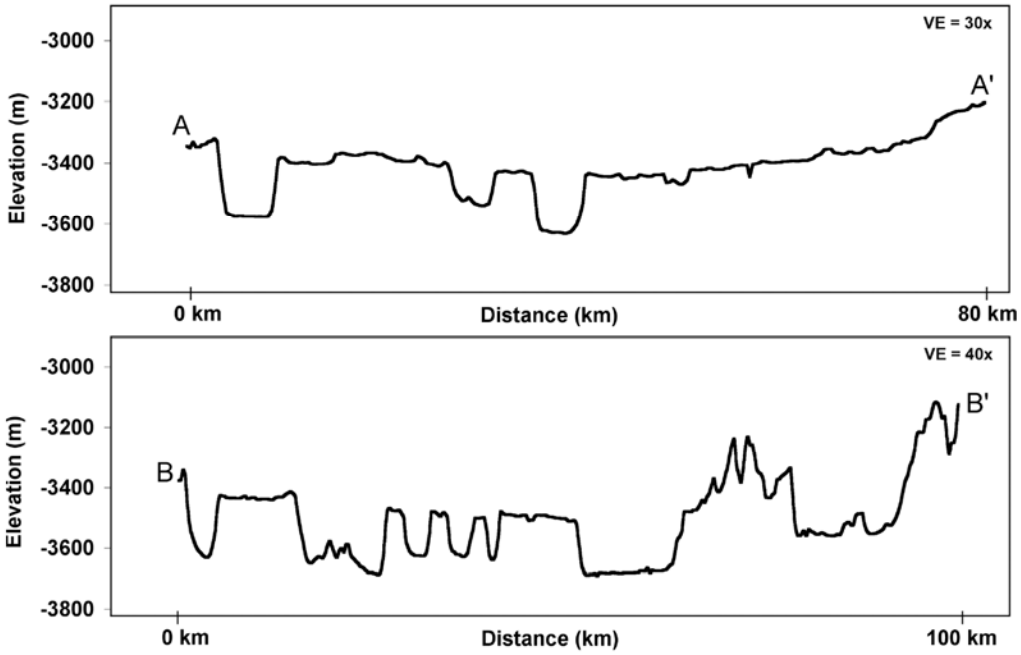

Figure DR2b

Figure DR2. A: CTX image P01_001520_1825_XN_02N016W displaying relevant image stamps and MOLA profile tracks discussed in the main text. B: MOLA profiles across the thermokarst depressions in crater Y.

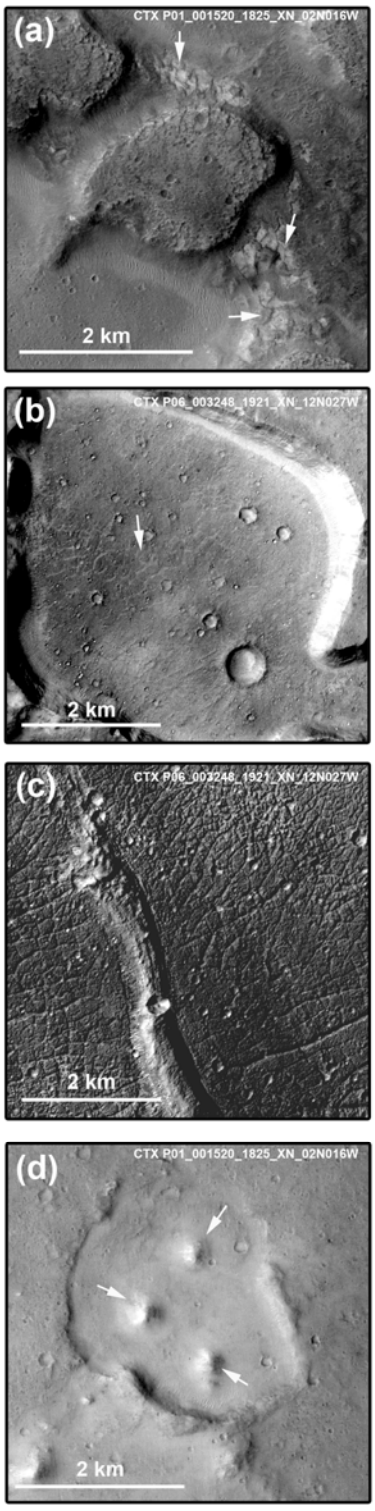

Figure DR3. a) CTX image displaying polygonal fractures on the floor of crater Y. Polygons in this location appear beneath a thin mantling deposit. (b, c) CTX images of polygons on the floors of thermokarst depressions in distal Ares Vallis. (d) CTX image of

mound forms within a thermokarst depression in crater Y. These mounds are morphologically similar to terrestrial pingos.

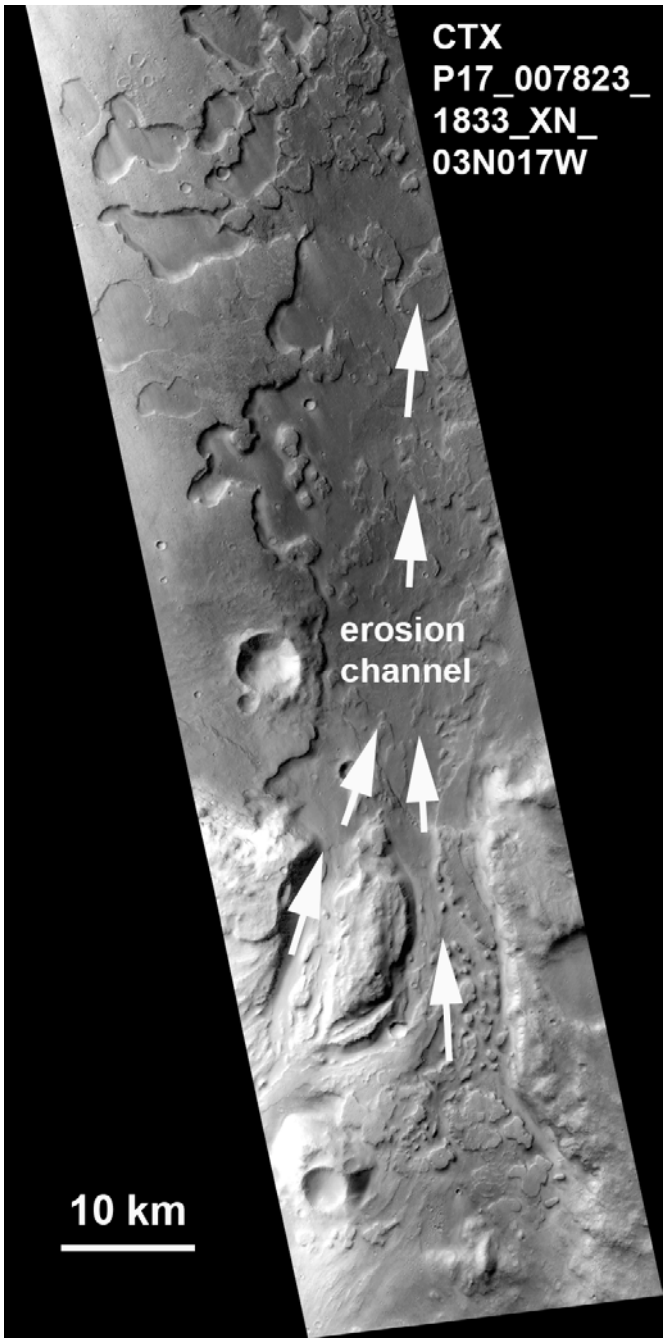

Figure DR4. CTX image P17_007823_1833_XN_03N017W. The eastern branch of Ares Vallis bisects and destroys the thermokarst terrain in crater Y. This suggests that thermokarst formation pre-dates the erosion of this channel. Crater statistics from the thermokarst terrain indicate a post-deposition surface age of ~3.30 Ga. This constrains the time of formation of the thermokarst features to some time during the height of fluvial activity within Ares Vallis.

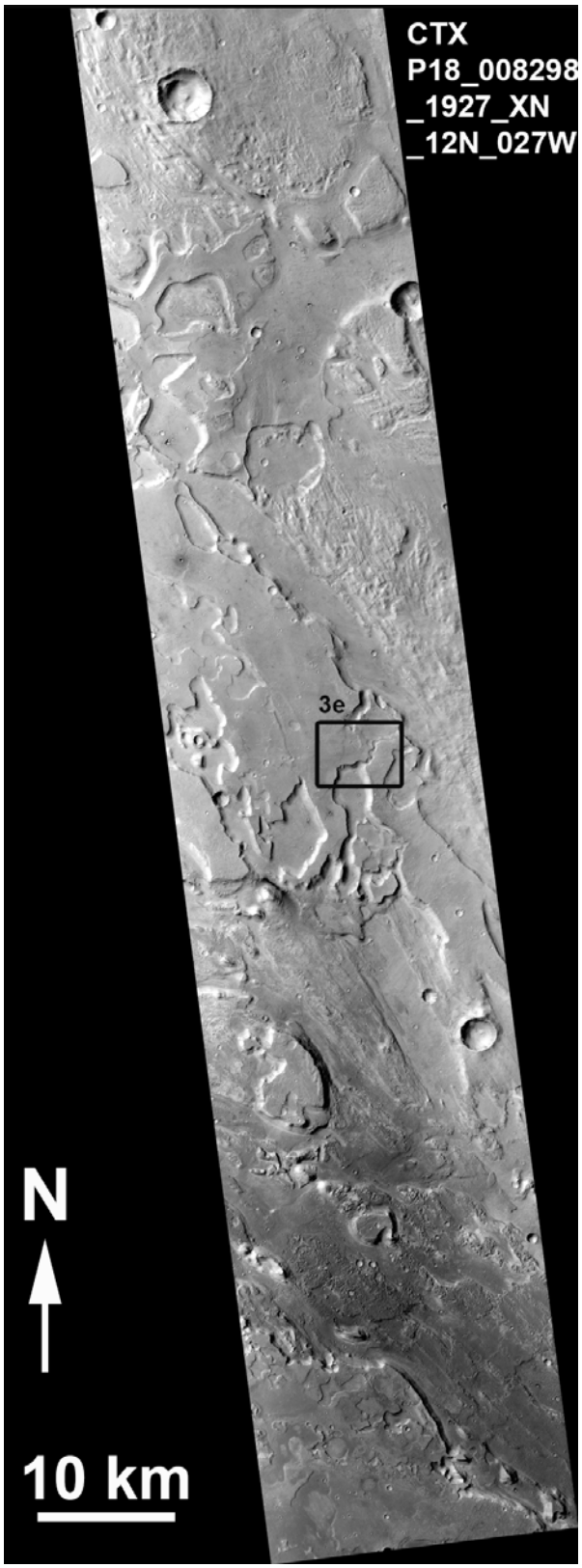

Figure DR5. CTX image P18_008298_1927_XN_12N027W of the thermokarst terrain in distal Ares Vallis. Image stamp for Fig. 3e is labelled.

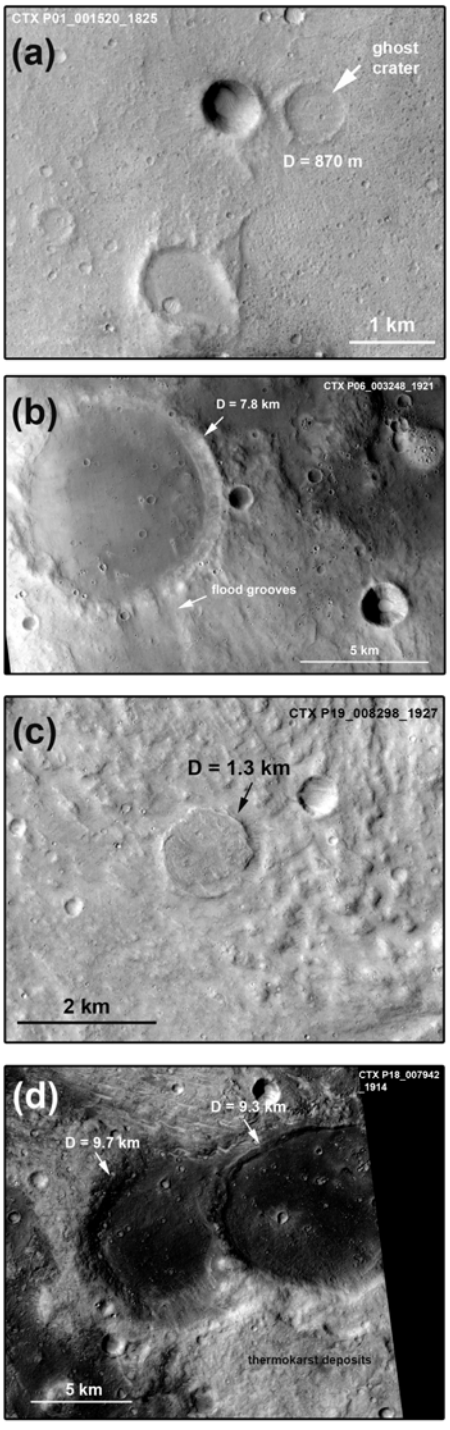

Figure DR6. (a) CTX image of a ghost crater (partially buried) on the floor of crater Y. (b –d) CTX images of partially destroyed craters in distal Ares Vallis. These craters are representative of older Noachian terrain that was exhumed during flood erosion. These craters are now partially buried by the thermokarst deposit.

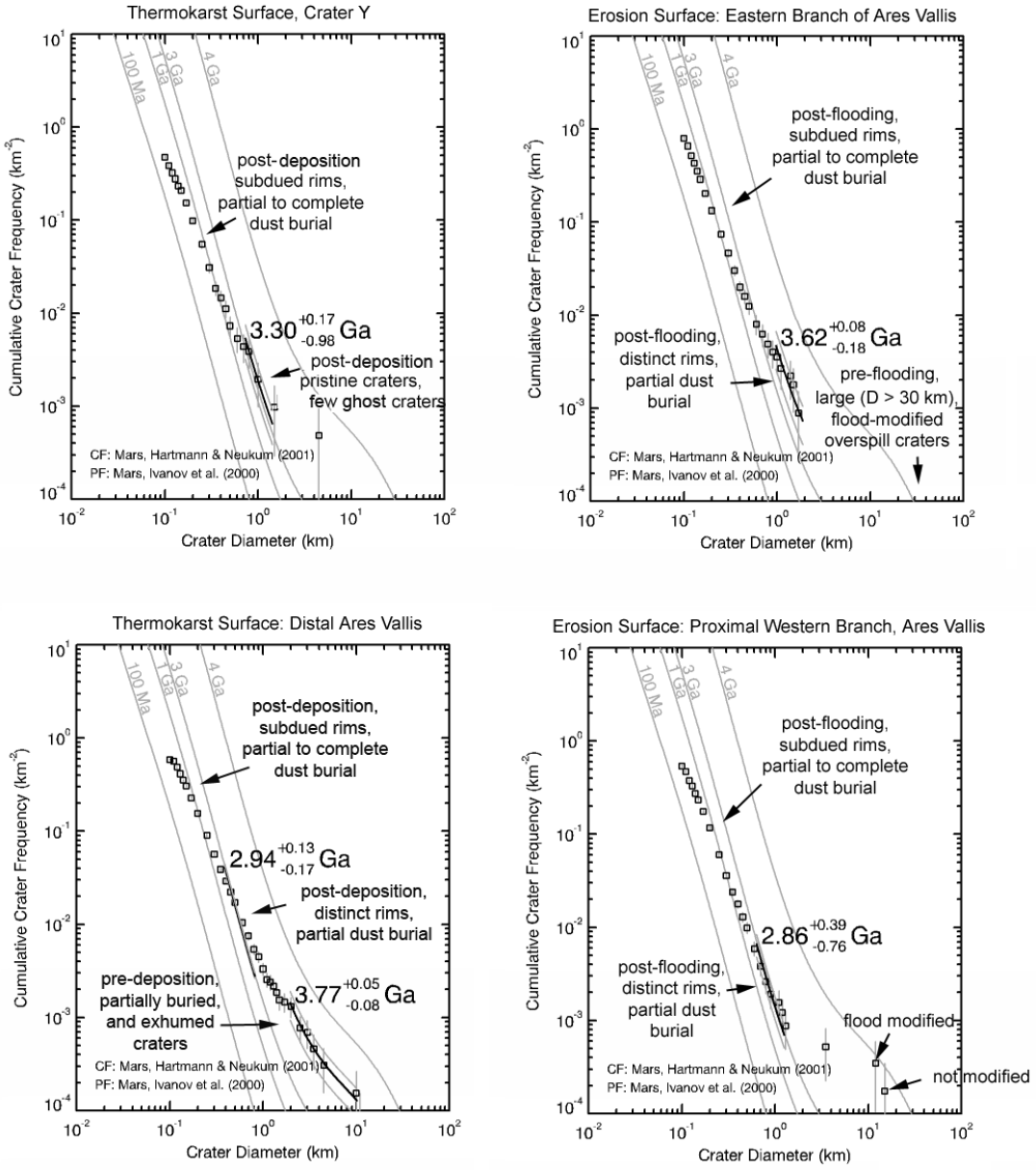

Figure DR7. Binned crater cumulative frequency plots for thermokarst and erosion surfaces in Ares Vallis. The general morphologic characteristics, relative age relationships to flooding, and modelled surface ages for specific crater populations are labelled. Plots indicate that deposition of the thermokarst units is temporally related to flood activity in Ares Vallis. Crater production and chronology functions were plotted following Ivanov (Ivanov, 2001) and Hartmann and Neukum (Hartmann and Neukum, 2001).

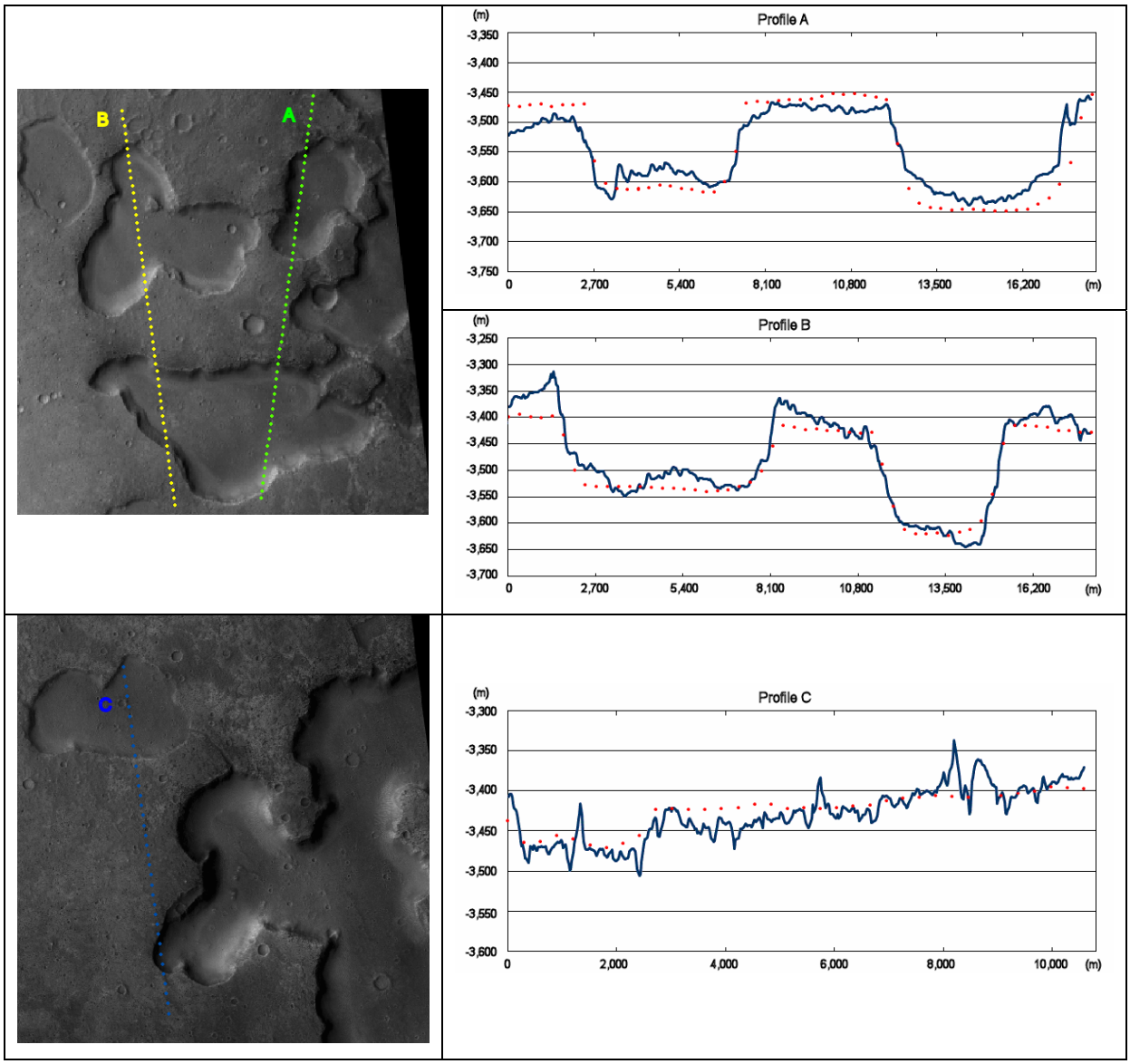

Figure DR8. DR8: Plots of CTX stereo DTM (all height grid-points) compared against the MOLA height points within 160 m of the MOLA pierce points.

1. CTX Digital Terrain Model construction methods

The NASA MRO (Mars Reconnaissance Orbiter) deploys two optical pushbroom CCD (Charge Couple Device) cameras that are capable of across-track stereo targeting. Both the CTX (Context Camera) and HiRISE (High Resolution Imaging Science Experiment) provide very high-resolution stereo imagery at 6 m and sub-metre (up to 20 cm) resolution respectively (Malin et al., 2007; Kirk et al., 2008). For some 10% of the total acquisitions, across-track stereoscopic observations can be acquired by HiRISE with a slightly higher (as yet unpublished) duty cycle from CTX. CTX is claimed to be acquired whenever HiRISE is acquired (R. Kirk, private communication, 2008) but inspection of the catalogue does not support this claim.

The thermokarst depressions in the target study area of this paper are covered by a CTX stereo pair, P01_001520_1825 and P17_007823_1833. The high SNR (signal to noise ratio > 100:1) and relatively high horizontal IFoV (Instantaneous Field of View) of ≈6m/pixel at 290km together with the 30km coverage (see the detailed sensor specification of CTX (Malin et al., 2007)), the target area is suitable for CTX stereo DTM construction. We employed our own stereo photogrammetric techniques that are based on a non-rigorous sensor model and hierarchical image-matching scheme. Further technical details are presented in Kim and Muller (2008, 2009).

A barrier to applying these stereo photogrammetric methods is a pointing oscillation in the direction of the stereobase (Kirk et al., 2003), the so-called “jitter effect”. In our experience with CTX imagery, the jitter effect is usually not as obvious as with MOC Narrow Angle imagery that was the technological predecessor of CTX provided by the same commercial supplier. However, since CTX image

P17_007823_1833 has twice the exposure time of its corresponding stereo mate (P01_001520_1825), the jitter especially at the end of the image scan is significant. To try to minimise any resulting DTM error from this jitter, we employed three approaches; 1) use of ISIS version 3 program, "spicefit" which applies a polynomial fitting on the pointing data; 2) use of a non-rigorous sensor model for the relatively small stereo coverage in order to smoothly interpolate the pointing errors; 3) Surface matching of the resultant stereo DTM product using MOLA height points employing the method of Lin et al. (2009) to reduce unresolved positioning error from the previous two approaches. The final DTM product when compared with MOLA spot elevations shows a reasonable agreement with the MOLA height profile (see below). The DTM has a grid-spacing of 18 m, and a theoretical vertical precision of 3 m, although it is quantised in 1m intervals.

2. Assessment of DTM height accuracy

To validate the CTX stereo DTM described in this paper, the MOLA orbits were corrected for bad orbits and occasional biases (Neumann et al., 2001). Height differences between the MOLA height points (ellipsoid height) and the CTX gridded DTM points were computed. A buffer distance of 160 m (equivalent to a MOLA laser footprint) was applied to the pierce point of each MOLA footprint and those CTX DTM points that intersected with the three transects (A, B and C in Figure 1) were chosen. The gridded DTM points of the CTX DTMs located in these buffered MOLA points were then selected and their height differences from MOLA computed. The results are shown in GSA Data Repository Table 1 listed below.

Table DR1: Statistics of height difference between MOLA height points and CTX stereo DTMs.

	No. of MOLA	Maximum (m)	Minimum (m)	Mean (m)	Std dev. (m)
Profile A	55	62.267	-62.419	-1.114	27.130
Profile B	54	44.141	-71.960	-12.351	21.098
Profile C	36	38.500	-71.750	1.361	19.628

The location of the MOLA height points and the associated profiles of the CTX DTM were then plotted in Figure DR8. This figure shows minimal height differences with no detectable bias. Moreover, it is also clearly demonstrated that the CTX stereo DTM is capable of resolving the detailed terrain relief.

3. Crater Count Methods

To refine the timing of thermokarst formation and the development of flood erosion surfaces in Ares Vallis we have obtained crater counts for D > 100 m from high resolution (6 m pix^{-1}) MRO context camera images (CTX). Previous crater ages have been defined in Ares Vallis for specific bedrock units and not for geomorphic units associated with flood resurfacing (Marchenko et al., 1998; Tanaka and Skinner, 2004). Our analysis is the first study to use high-resolution crater statistics to resolve the timing of flood erosion and deposition within Ares Vallis. Furthermore, with the crater counts and from cross-cutting/superposition relationships, we were able to constrain when the thermokarst features formed relative to flood erosion in Ares Vallis.

In our analysis we utilized the crater counting and dating techniques employed and established by (Hartmann and Neukum, 2001; Ivanov, 2001; Hartmann, 2005) to provide relative and absolute ages for the thermokarst and flood erosion surfaces. Counts

were made using the Mars Editing and Assessment toolset (Simpson et al., 2008). This visual basic application allows craters to be tagged and measured on an image mosaic backdrop, while saving relevant diameter and location data to an ESRI shapefile. Crater statistics are presented as crater densities for N(0.1), N(0.5), and N(1) (where N represents the cumulative number of craters counted for 10^6 km^2) and on $\log_{10}$ cumulative frequency plots (Hartmann and Neukum, 2001). The freeware program Craterstats was used to plot the crater statistics and to fit isochrons (with error) to determine the absolute age of the flood surfaces (Michael and Neukum, 2008). For this analysis, all randomly distributed impact craters on the surfaces were counted. Non-randomly distributed secondary craters found in chains or clusters were excluded. Most recently, it has been concluded that the majority of randomly distributed impact craters < 1 km in diameter are primary in origin with contamination by secondary impacts at < 10 % of the total measured (Hartmann, 2007; Hartmann et al., 2008). It was concluded by these authors that age determination from the small impact crater population is a useful method for surfaces with limited aerial exposure and limited abundance of large diameter impact craters.

We assumed that the flood erosion associated with Ares Vallis was responsible for complete resurfacing of craters exposed on older bedrock units in the flood erosion channels. The depths (d) of erosion channels (200 m – 2 km) were used to determine the critical diameter below which craters were removed by flooding. Using established impact crater d:D ratios for simple (D < 6 km) and complex (D > 6 km) craters on Mars (Garvin et al., 1999), we predicted that craters with D < 70 km should be completely incised by flood erosion in the proximal and medial Ares Vallis regions. The broad range

in critical values for D is dependent on the craters's location on the surface before the flood (e.g. within a channel, proximal or distal to the flood source, behind an obstacle), the magnitude of the flood event, and the resistance of the crater wall to erosion. From morphologic analysis of craters on the flood erosion channel surfaces, we have determined that all craters < 2 km in diameter post-date flooding and provide a post-flood crater retention age. These post-flood impact craters have distinct ejecta blankets, sharp rims, and superimpose flood grooves. Crater retention ages could not be determined from the smallest crater populations (D < 750 m +- 150 m) due to long term obliteration processes that cause a steady reduction in slope of the cumulative frequency curves below established production functions.

For the thermokarst surfaces, crater cumulative frequency curves indicate post-deposition and pre-deposition ages (Fig. DR7). For the deposits in crater Y, few buried (ghost) craters were identified. These ghost craters (Fig. DR6), with diameters ~ 700 m – 2 km, represent a pre-deposition surface and indicate a sediment thickness of ~ 115 m – 330 m. This thickness estimate is consistent with the measured depths of the thermokarst depressions. The majority of impact craters on the crater Y thermokarst surface superimpose the deposit, have fresh crater rims, and exhibit obvious ejecta blankets. This population is representative of a post-deposition age, modelled at 3.3 Ga. In distal Ares Vallis, the thermokarst terrain overlies flood grooves indicating an earlier period of flood erosion followed by deposition. Exhuhmed large diameter impact craters (D > 2 km) are evident on the grooved surface and likely represent older flood modified Noachian terrain (Fig. DR6). For D < 2 km the crater frequency curve does not follow established isochrons and dips below the 3 Ga production function (Fig. 4). The effect of crater

obliteration by Mars weathering processes likely contributes to the lack of fit of the smaller diameter craters to the production curves for all surfaces. This effect may be particularly enhanced on flood sediments that are softer relative to the bedrock-lined erosion channels. This hypothesis is confirmed by a comparison between values of N(0.1) for crater Y fill materials and N(0.1) for the eastern branch erosion channel (Table 1).

The timing of formation of the individual thermokarst features can be constrained by the cross-cutting relationships with the crater Y erosion channel. The eastern boundaries of the channel-proximal thermokarst depressions are obliterated by the erosion channel (Fig. DR4). This indicates that flood erosion was occurring within crater Y after the sediments containing the thermokarst features were deposited and after the thermokarst depressions were formed. This allows us to constrain the timing of thermokarst formation to ~ 3.6 – 3.0 Ga by comparison to the crater statistics from the depositional and erosional surfaces. The bisected sediments within crater Y likely represent deposits from an earlier stage of flooding that filled crater Y with water.

GSA Data Repository References

http://wwwflag.wr.usgs.gov/ISIS/.

Garvin, J.B., Sakimoto, S.E.H., Schnetzler, C., and Frawley, J.J., 1999, Global geometric properties of Martian impact craters: A preliminary assessment using Mars Orbiter Laser Altimeter (MOLA), 5th International Conference on Mars.

Hartmann, W.K., 2005, Martian cratering 8: Isochron refinement and the chronology of Mars: Icarus, v. 174, p. 294-32010.1016/j.icarus.2004.11.023.

—, 2007, Martian cratering 9: Toward resolution of the controversy about small craters: Icarus, v. 189, p. 274-27810.1016/j.icarus.2007.02.011.

Hartmann, W.K., and Neukum, G., 2001, Cratering Chronology and the Evolution of Mars: Space Science Review, v. 96, p. 165-194.

Hartmann, W.K., Neukum, G., and Werner, S., 2008, Confirmation and utilization of the "production function" size-frequency distributions of Martian impact craters: Geophysical Research Letters, v. 3510.1029/2007gl031557.

Ivanov, B., 2001, Mars/Moon Cratering Rate Ratio Estimates: Space Science Reviews, v. 96, p. 87-104.

Kim, J.-R., and Muller, J.-P., 2008, Very high-resolution stereo DTM extraction and its application to surface roughness estimation over Martian surface.: International Archives of Photogrammetry, Remote Sensing and Spatial Information Sciences, v. 37, p. 993-998.

—, 2009, Multi-resolution topographic data extraction from Martian stereo imagery: Planetary and Space Science, p. in press.

Kirk, R.L., Howington-Kraus, E., Redding, B., Galuszka, D., Hare, T.M., Archinal, B.A., Soderblom, L.A., and Barrett, J.M., 2003, High-resolution topomapping of candidate MER landing sites with Mars Orbiter Camera narrow-angle images: Journal of Geophysical Research-Planets, v. 10810.1029/2003je002131.

Kirk, R.L., Howington-Kraus, E., Rosiek, M.R., Anderson, J.A., Archinal, B.A., Becker, K.J., Cook, D.A., Galuszka, D.M., Geissler, P.E., Hare, T.M., Holmberg, I.M., Keszthelyi, L.P., Redding, B.L., Delamere, W.A., Gallagher, D., Chapel, J.D., Eliason, E.M., King, R., and McEwen, A.S., 2008, Ultrahigh resolution topographic mapping of Mars with MRO HiRISE stereo images: Meter-scale slopes of candidate Phoenix landing sites: Journal of Geophysical Research-Planets, v. 113E00a24 10.1029/2007je003000.

Lin, S.Y., Muller, J.-P., Mills, J., and Miller, P., 2009, An assessment of surface matching for the automated co-registration of MOLA, HRSC and HiRISE DTMs.: Earth and Planetary Science Letters, p. in review.

Malin, M.C., Bell, J.F., Cantor, B.A., Caplinger, M.A., Calvin, W.M., Clancy, R.T., Edgett, K.S., Edwards, L., Haberle, R.M., James, P.B., Lee, S.W., Ravine, M.A., Thomas, P.C., and Wolff, M.J., 2007, Context Camera Investigation on board the Mars Reconnaissance Orbiter: Journal of Geophysical Research-Planets, v. 11210.1029/2006je002808.

Marchenko, A.G., Basilevsky, A.T., Hoffman, H., Hauber, E., Cook, A.C., and Neukum, G., 1998, Geology of the common mouth of the Ares and Tiu Valles, Mars: Solar System Research, v. 32, p. 425-452.

Michael, G., and Neukum, G., 2008, Surface dating: software tool for analysing crater size-frequency distributions including those showing partial resurfacing events, Proc. of the Lun. and Planet. Sci. Conf. XXXIX.

Neumann, G.A., Rowlands, D.D., Lemoine, F.G., Smith, D.E., and Zuber, M.T., 2001, Crossover analysis of Mars Orbiter Laser Altimeter data: Journal of Geophysical Research-Planets, v. 106, p. 23753-23768.

Simpson, J.I., Kim, J.R., and Muller, J.-P., 2008, 3D crater database production on Mars by automated crater detection and data fusion, The International Congress of the Photogrammetry, Remote Sensing and Spatial Information Sciences, Volume Vol. XXXVII. Part B4: Beijing, p. 1049-1054.

Tanaka, K.L., and Skinner, J.A., 2004, Advances in reconstructing the geologic history of the Chryse region outflow channels on Mars, Proceedings of the Lunar and Planetary Science Conference XXXV Abstract #1770.